CPW Meander Line MIMO Antenna Loaded with Metallic Stubs to Enhance Isolation and Reduce Mutual Coupling

Ajay Kumar[1], and Bappadittya Roy[2,*]
[1]School of Electronics Engineering, VIT-AP University, Amaravati 522241, Andhra Pradesh, India
[2]School of Electronics Engineering, VIT-AP University, Amaravati 522241, Andhra Pradesh, India

*Corresponding author: Bappadittya Roy (bappadittya.roy@vitap.ac.in)

ABSTRACT A compact four-port MIMO antenna is proposed for the 2.4 GHz ISM band and wireless communication applications. The antenna occupies a compact footprint of $0.372\lambda_0 \times 0.372\lambda_0$ and is implemented on an FR4 substrate with a dielectric constant of $\varepsilon_r = 4.4$. Initial antenna design study for unidirectional radiation and high frequency band. Ultimately, a CPW antenna featuring with menderline is designed for unidirectional to lower frequency resonances. A coplanar waveguide (CPW) feeding scheme is employed, and inter-element isolation to enhanced through the antenna's inherent self-isolation upto -24 dB and reduce mutual coupling. Further improved by integrating a strategically positioned parasitic element between the radiating elements, achieving a peak isolation of 27 dB. The design offers a measured peak gain of 2.83 dBi and a radiation efficiency of 96%. It covers an impedance bandwidth of 1.81–3.37 GHz with a minimum return loss of 49 dB. MIMO diversity analysis confirms an envelope correlation coefficient (ECC) below 0.01, a diversity gain (DG) of 9.99 dB, a channel capacity loss (CCL) of 0.36 bits/s/Hz, and a mean effective gain (MEG) less than -3 dB, all within standard performance limits. The fabricated prototype was experimentally validated through S-parameter, radiation pattern, and gain measurements, which exhibit good agreement with the corresponding simulated results, thereby validating the proposed antenna's suitability for high-performance ISM-band wireless communication applications.

INDEX TERMS MIMO, Menderline, Coplanar waveguide (CPW), Isolation, Envelope correlation coefficient (ECC),Channel capacity loss (CCL).

I. INTRODUCTION

Multi-Input Multi-Output (MIMO) innovations have revolutionized wireless communication by enabling simultaneous data transmission over multiple spatial channels, dramatically enhancing spectral efficiency, channel capacity, and link reliability while using the same frequency resources. Unlike traditional single-antenna systems, MIMO leverages spatial diversity to combat multi path fading, which is especially beneficial in dense, reflective environments common to urban and indoor applications. Given the rapid proliferation of wireless devices and the limited availability of licensed spectrum, MIMO has become an indispensable tool for meeting high throughput and reliability demands in emerging wireless networks [1], [2]. The Industrial, Scientific, and Medical (ISM) band that spans from 1.84 to 3.62 GHz is accessible globally, operates without licensed restrictions, and is extensively used in a wide range of applications including IoT sensors, smart healthcare systems, wearable devices, and home automation networks. The moderate frequency range enables physically compact antenna designs suitable for miniature devices while still offering adequate propagation characteristics. However, designing MIMO antennas to operate effectively across this entire ISM spectrum requires careful attention to wideband impedance matching, radiation performance, and stable patterns—all of which become increasingly complex in compact, multi-element configurations [3]–[5]. When integrating four antenna elements into a tightly constrained layout necessary for compact gateway devices, wearable gadgets, or handheld sensors—the mutual electromagnetic coupling between elements becomes a serious impediment to performance. This coupling results in decreased isolation, elevated envelope correlation coefficient (ECC), distorted far-field patterns, and diminished diversity and efficiency, effectively eroding MIMO benefits. The challenge is particularly acute in wideband designs covering the full ISM range, where coupling must be mitigated consistently across the entire frequency span [6]–[8]. To address mutual coupling, several decoupling mechanisms have been developed. Defected Ground Structures (DGS) introduce patterned perturbations in the ground plane to create bandstop filtering effects, reducing coupling. While effective, DGS designs can complicate the fabrication process, restrict design flexibility, and sometimes degrade radiation performance [9], [10]. Neutralization lines connect adjacent radiating elements with reactive lines that introduce phase-canceling currents, improving isolation in narrowband designs; however, they often lack the bandwidth breadth needed for ISM band coverage and require precise tuning [11], [12]. Recent studies have focused on the development of compact MIMO antennas for 5G and beyond wireless communication systems. Muttair *et al.* proposed a wide and multi-band 2×2 MIMO antenna for 5G mmWave applications, demonstrating enhanced bandwidth and multi-band characteristics suitable for high-frequency communication systems [13]. Subsequently, an ultra-small 8×8 massive MIMO antenna was introduced for future 6G wireless devices, achieving high isolation and improved MIMO performance within a compact footprint [14]. Fractal-based 4×4 MIMO array antennas have also been investigated to improve bandwidth and radiation characteristics for emerging 6G applications [15]. Furthermore, a compact multi-band MIMO antenna geometry was reported to support both 5G and 6G wireless systems while maintaining satisfactory impedance matching and isolation performance [16]. In addition, wide and multi-band MIMO antenna designs have been developed to enhance bandwidth and diversity performance for 5G communication systems [17]. Although these studies demonstrate significant advancements in compact and multi-band MIMO antenna designs, challenges related to achieving a compact footprint, simple antenna geometry, and enhanced inter-element isolation remain. Motivated by these challenges, this work proposes a compact CPW-fed meander-line four-port MIMO antenna employing parasitic stubs to achieve improved isolation while maintaining excellent impedance matching and MIMO diversity performance. Electromagnetic Band-Gap (EBG) structures and metamaterials present another decoupling strategy by creating periodic surfaces that suppress surface waves and coupling. Although they can provide substantial isolation over wide frequency ranges, their typically sizeable periodic unit cells and required number of periods complicate integration into space-constrained modules [18], [19]. Altering the physical orientation of antennas through spatial or polarization orthogonality is an alternative geometric method of reducing correlation and coupling; nevertheless, practical considerations such as device footprint or ergonomic requirements may limit the effectiveness of purely geometric approaches [20], [21]. In contrast, parasitic-element decoupling offers a compelling and adaptable solution. By placing strategically designed passive structures such as stub resonators, slots, loops, or patches—in proximity to active elements, one can induce out-of-phase coupling currents that counteract mutual interference, thereby improving isolation. Critically, these parasitic elements can be tuned across a wide frequency span by adjusting their geometric parameters such as length, width, shape, position, and orientation. This parametric flexibility enables simultaneous wideband matching, isolation, and radiation performance without substantially increasing the antenna footprint [22]–[25]. A combined approach utilizing orthogonal arrangement for geometric diversity and parasitic elements for targeted coupling suppression creates a powerful hybrid architecture. This synergy yields compact, wideband MIMO systems that simultaneously tackle footprint limitations and inter-element interference.

Recent work in parasitic-assisted beamforming and hybrid decoupling strategies underscores the potential for reconfigurable, high-performance MIMO antennas in future wireless platforms [26]. Although CPW-fed antennas, meander-line structures, and parasitic decoupling techniques have been individually investigated in previous studies, their combined implementation in a compact four-port orthogonal MIMO configuration without employing DGS or EBG structures has received limited attention. The proposed antenna integrates these techniques through systematic co-design to simultaneously realize compact size, wide impedance bandwidth, high isolation, and excellent MIMO diversity performance using a simple planar structure suitable for low-cost fabrication. In this study, we introduce a four-port orthogonal MIMO antenna system tailored to the 1.81–3.27 GHz ISM band. The design incorporates parametrically optimized parasitic stubs deployed adjacent to each radiating element. Through meticulous electromagnetic simulations and sequential parametric tuning, the stub geometry and placement are optimized to achieve isolation levels better than -27 dB across the operating band, while ensuring an ECC below 0.01, stable gain and radiation patterns, and high efficiency.The resulting design demonstrates excellent performance in both simulated and measured evolutions, positioning it as a practical solution for compact IoT and wearable applications demanding robust MIMO operation.

The remainder of this discussion is structured as follows. Section II provides a detailed description of the antenna geometry, configurations with parasitic-stub, orthogonal layout, and parametric tuning methodology. Section III presents comprehensive simulation and measurement results including scattering parameters, radiation patterns, gain, ECC, diversity gain, and efficiency. Section IV summarizes the conclusions and outlines directions for future multidisciplinary enhancements such as dual-band operation and mechanical flexibility.

II. ANTENNA MECHANISM AND DESIGN VERIFICATION

The proposed single monopole antenna exited using a coplanar feed isolation. Full design methodology mentioned as length e and width f, optimized for 50 Ω impedance matching. A horizontal conductive strip is integrated above the feed line, serving as an intermediate coupling section. Two inverted L-shaped stubs are symmetrically attached to the horizontal strip, each separated from the feed line by a gap s and make a CPW full structure. Each stub consists of a horizontal segment of length b and a vertical segment of length h, such that the total stub length is $b + h$. The stub widths are fixed at 0.5 mm and optimized to improve impedance bandwidth and enhance isolation. The CPW feed is designed with a gap of 2 mm between the feed conductor and each ground plane, and a ground-plane height of c, to achieve the desired 50 Ω impedance. This configuration supports wideband operation,

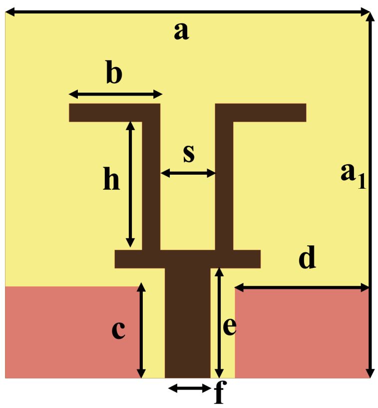

(a)

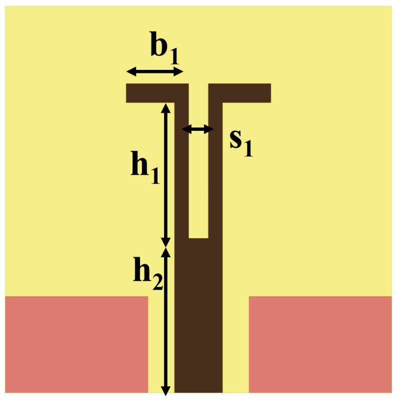

(b)

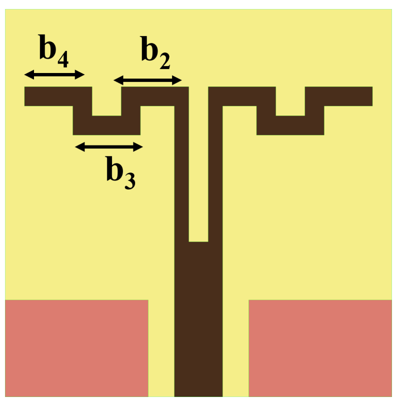

(c)

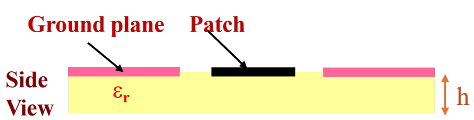

(d)

FIGURE 1: Progression of CPW single antenna Design steps (a) step-1, (b) step-2, (c) step-3 and (d) side view: The antenna dimensions are: $a = 20$, $a_1 = 20$, $b = 5$, $c = 5$, $d = 7.4$, $e = 6$, $f = 2.5$, $h = 7$, $s = 3$, $s_1 = 1$, $b_1 = 3.25$, $h_2 = 8$, $h_1 = 7$, $b_4 = 3.5$, $b_2 = 3.5$, and $b_3 = 3.5$ mm (all dimensions in millimetres).

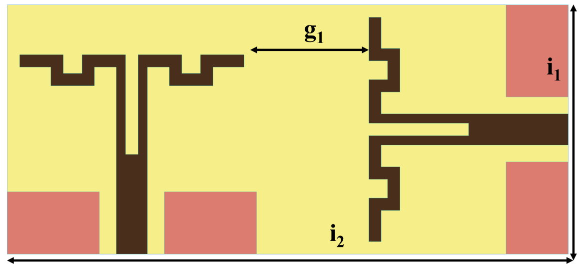

FIGURE 2: Two-port MIMO antenna with optimized spacing parameters: $i_1 = 20$ mm, $i_2 = 45$ mm, and $g_1 = 10$ mm.

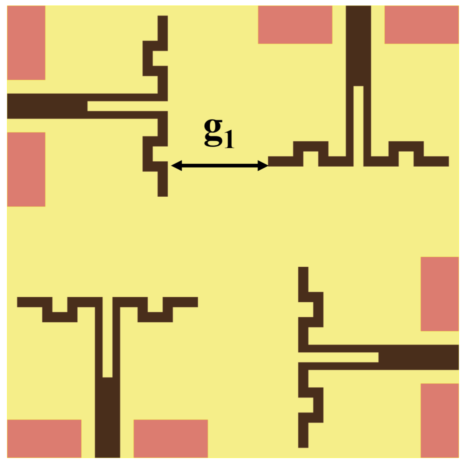

FIGURE 3: Four-port MIMO antenna without isolation elements

with the prototype resonating at 4.5GHz however, the design does not fully cover the ISM band at 2.48 GHz. The overall configuration is illustrated in Figure. 1a. To shift the resonant frequency to a lower value, the horizontal stub was removed and the spacing between the inverted L-shaped stubs were modified to s_1. The entire length of each inverted L-shaped stub was set to $h_1 + b_1$, and the feed length was increased to h_2. This modified structure is shown in Figure. 1b. The antenna resonates at 3.97 GHz indicating a return loss of 29 dB. However, it still does not achieve the targeted ISM band at 2.4 GHz. To further shift the operating frequency to the desired ISM band, a meander line structure is employed in the antenna design to achieve miniaturization by increasing the electrical length without enlarging the physical size. This technique enables the antenna to resonate at the desired frequency while maintaining a compact footprint, making it suitable for portable and integrated systems. Moreover, the meander line contributes to impedance matching and can support multiband operation due to the multiple current paths introduced by the bends. a meander line was attached to the horizontal strip, as indicated in Figure. 1c, without making any changes to the antenna ground plane or the spacing s between the inverted L-shaped stubs. This modification enables the antenna to achieve an impedance bandwidth from 1.63 GHz to 3.46 GHz, with a resonant frequency at 2.4 GHz and a return loss of 33 dB. This bandwidth covers the ISM band, making the antenna suitable for both ISM and wireless communication applications. Figure.1d shows the side view of the single antenna.

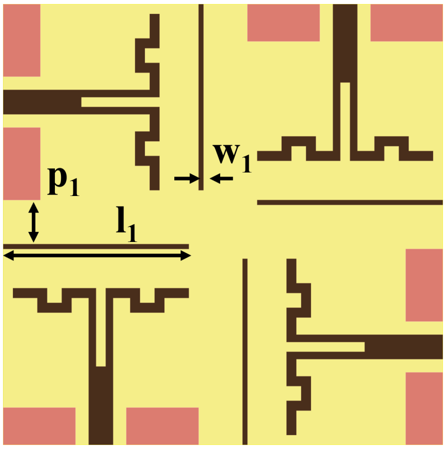

FIGURE 4: Suggested four-port MIMO antenna with isolation elements. Antenna dimension parameters: $w_1 = 0.5$ mm, $l_1 = 19$ mm, $p_1 = 1$ mm.

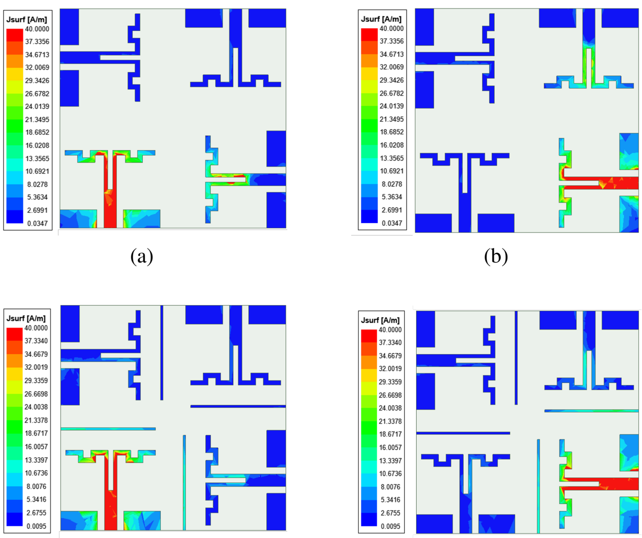

(a) (b) (c) (d)

FIGURE 5: Surface current distribution of the proposed four-port MIMO antenna at 2.48 GHz: (a) Port 1 excited without isolation element, (b) Port 2 excited without isolation element, (c) Port 1 excited with isolation stub, and (d) Port 2 excited with isolation stub.

A. TWO-ELEMENT ANTENNA DESIGN & CONFIGURATION

The two-element antenna layout is developed by arranging two identical single-element antennas in an orthogonal orientation with an edge-to-edge spacing of g_1 as shown in Figure. 2. The lengths and widths of the overall antennas are denoted as i_1 and i_2, respectively. The orthogonal arrangement is adopted to maintain a compact footprint while enhancing isolation through spatial diversity. With the optimized spacing, the antenna is designed to resonate at 2.59 GHz with an input return loss of approximately 38 dB and a measured mutual coupling of 38 dB between the antenna elements, which is considered acceptable. The theoretical minimum edge-to-edge separation required to achieve minimal coupling can be expressed as [27].

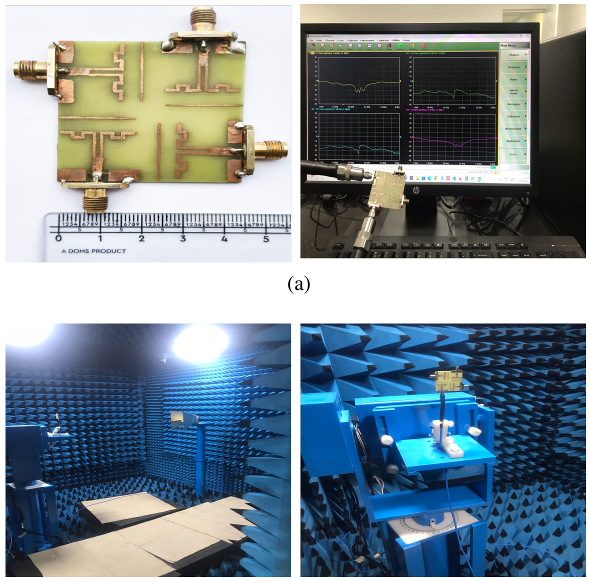

(a)

(b)

FIGURE 6: (a) Prototype depicting top and bottom views (b) Antenna testing using VNA and anechoic chamber

$$g = \frac{\lambda_{\max}}{2} = \frac{c}{2f_{\min}}, \tag{1}$$

where $c = 3 \times 10^8$ m/s is the speed of light, and $f_{\min} = 2.59$ GHz is the lowest operating frequency. Substituting these values yields $\lambda_{\max} \approx 115.83$ mm, resulting in $g \approx 57.92$ mm. However, due to compact design constraints, the actual edge-to-edge spacing is optimized to $g_1 = 10$ mm through parametric analysis to achieve mutual coupling reduction. This corresponds to less than a quarter-wavelength ($\lambda/4$) separation, which is sufficient to achieve acceptable isolation and spatial diversity in a compact form factor.

B. 2×2 *MIMO ANTENNA CONFIGURATION*

The two-port antenna was expanded to a four-port configuration with an optimized edge-to-edge spacing of $g_1 = 10\,\text{mm}$. The four radiating elements are arranged orthogonally to exploit spatial diversity and maintain a compact footprint, as illustrated in Figure. 3. This arrangement enhances self-isolation between antenna elements, achieving better than -24 dB isolation across the entire operating band. The suggested four-port antenna resonates at 2.48 GHz within the ISM band while maintaining high isolation performance. To further enhance the isolation between the antenna elements,

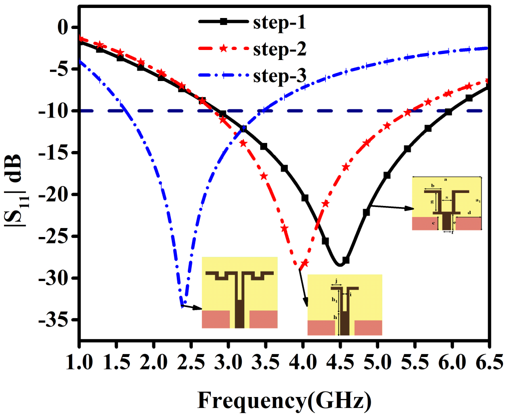

FIGURE 7: Progressive evolution of simulated results for the single-element antenna design

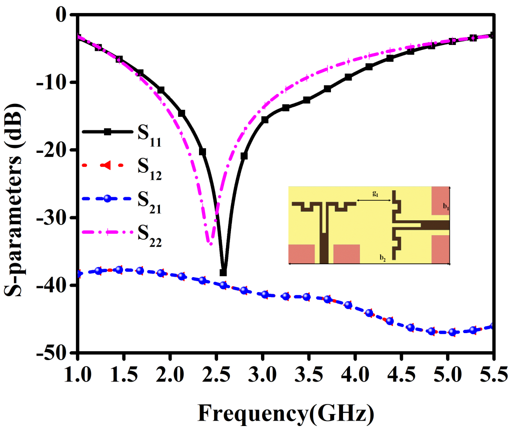

FIGURE 8: Simulated S-parameter results of the two-element antenna with an optimized inter-element spacing of 10 mm.

a parasitic element illustrated as a stub is introduced on the radiator surface, as illustrated in Figure. 4. This stub acts as an electromagnetic decoupling structure by disturbing the surface current distribution, thereby reducing mutual coupling between the ports. The position of the stub, denoted as p_1, is analyzed through a parametric study where p_1 is varied from 1 mm to 3 mm. After careful optimization, the value of $p_1 = 1$ mm is selected as it offers the best trade-off between isolation improvement and antenna impedance matching. At this optimized position, the antenna exhibits enhanced resonance behavior within the ISM band and improved isolation performance. In addition to the position, the geometric dimensions of the stub are also optimized to achieve optimal performance. The length of the stub, l_1, is varied from 17 mm to 20 mm, with 19 mm identified as the optimal length providing a significant contribution to isolation enhancement without adversely affecting the antenna bandwidth. Similarly, the width of the stub, w_1, is optimized between 0.4 mm and 1 mm, and an optimized width of 0.5 mm is chosen. These specific dimensions enable the stub to effectively suppress

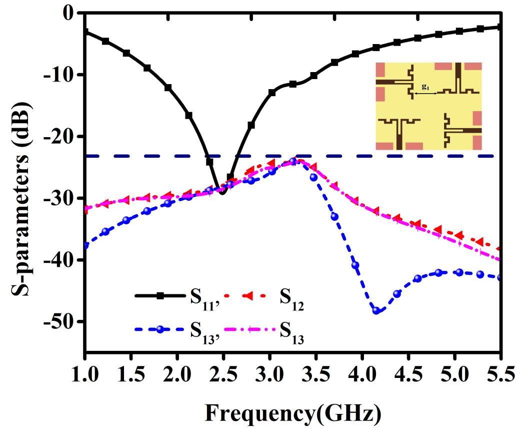

FIGURE 9: Four-port MIMO antenna without isolation elements

surface currents responsible for mutual coupling, thus improving the overall isolation level to approximately −27 dB. Moreover, the optimized stub geometry helps maintain the antenna's impedance bandwidth and radiation characteristics, ensuring it remains well-suited for reliable operation within the 2.4 GHz ISM band. The metallic stub functions as a parasitic resonator that electromagnetically interacts with the fields generated by the excited antenna element. When a port is excited, the stub supports induced currents that generate an opposing electromagnetic field, thereby interrupting the primary surface-current propagation toward the adjacent radiating elements. This redistribution of the surface current suppresses the dominant coupling paths and reduces the transfer of electromagnetic energy between neighboring ports. Consequently, the mutual coupling is significantly reduced while preserving the impedance matching and radiation characteristics of the antenna. The effectiveness of this mechanism is verified by the surface current distributions shown in Fig.5, where the current intensity on the adjacent elements is considerably lower after introducing the metallic stub. In the case without isolation elements Figure. 5(a) and 5(b), when Port 1 and Port 2 are excited respectively, significant surface currents propagate toward the neighboring radiating elements. This creates prominent coupling paths between the excited port and the adjacent elements, leading to reduced isolation. Conversely, with the inclusion of the isolation stub Figure. 5(c) and 5(d), for both Port 1 and Port 2 excitation, the surface currents are predominantly confined to the driven patch and feedline. The induced currents on adjacent elements are notably suppressed, and the high-intensity regions along potential coupling paths are diminished. This behavior confirms that the stub functions as a parasitic decoupling element, effectively altering the current distribution and mitigating inter-element coupling.

III. PERFORMANCE ANALYSIS AND DISCUSSION

The prototype of the intended four-port antenna, displaying top view is and Performance evaluation was conducted using

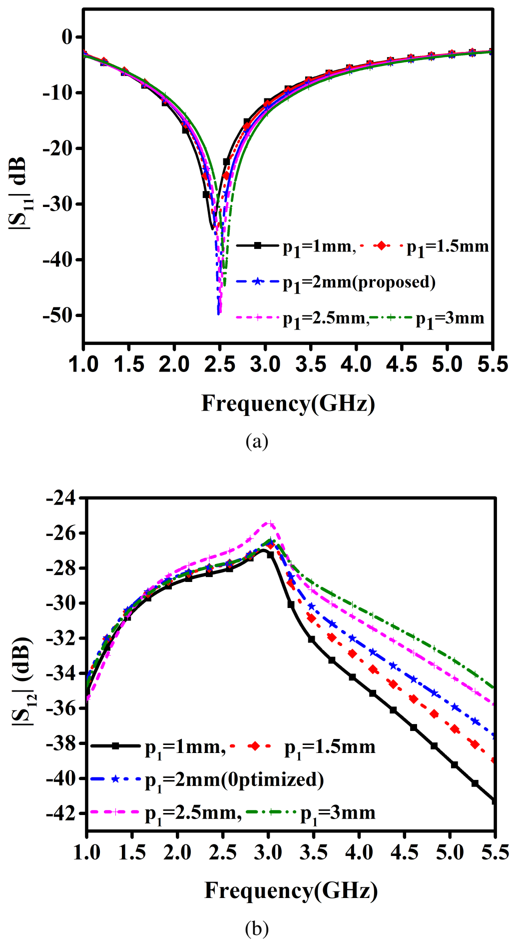

FIGURE 10: (a) Reflection coefficient results of parametric analysis for p_1 from 1 mm to 3 mm. (b) S_{12} parameters of the proposed antenna.

an MS46122B vector network analyzer (VNA) to obtain the necessary S-parameter measurements is shown in Figure. 6a. Subsequently, the antenna was tested within an anechoic chamber, as illustrated in Figure. 6b, to accurately characterize its radiation pattern and gain. The design evolution of the single monopole antenna is portrayed in Figure. 7. In the initial configuration (step-1), the antenna exhibits an operating bandwidth from 2.87 GHz to 5.97 GHz, achieving a return loss of 28 dB at 4.5 GHz. To achieve the targeted frequency band operation at 2.4 GHz, the second configuration (step-2) was developed, resonating from 2.80 GHz to 5.44 GHz with a prominent resonance at 3.97 GHz and an impedance bandwidth corresponding to a return loss of 29 dB. Further structural modifications led to the third configuration (step-3), operates throughout the frequency range of 1.6 GHz to 3.46 GHz, achieving a deep resonance at 2.4 GHz with a return loss of 33 dB. The progressive evolution demonstrates the tuning of the antenna geometry to meet the desired frequency specifications. Figure. 8 presents the simulated results of the two-element antenna configuration, where the inter-element spacing is optimized to 10 mm. The simulation indicates that the antenna operates over the frequency spans from 1.81 GHz to 3.82 GHz, with a pronounced resonance at 2.59 GHz, achieving a return loss of 38 dB. Furthermore, the mutual coupling (S_{21}) between the antenna elements is significantly reduced, reaching a value of -38 dB. Figure. 9 illustrates the simulated S-parameters of the suggested four-port MIMO antenna in the absence of any decoupling or isolation elements. The results indicate that the antenna resonates at 2.48 GHz with an impedance bandwidth (defined for $S_{11} \leq -10$ dB) ranging from 1.76 GHz to 3.49 GHz. A resonance is observed at 2.48 GHz, achieving a return loss of 29 dB, which confirms excellent impedance matching at the desired ISM band. Despite the absence of isolation structures, the simulated inter-element isolation remains below -24 dB across the operating band, demonstrating inherently reduced mutual coupling owing to the orthogonal positioning of the radiating elements and the physical separation between them. This performance provides a strong baseline for further enhancement through the integration of dedicated isolation techniques. Figure 10a depicts the reflection coefficient obtained from the parametric analysis of the stub position (p_1). The results indicate that placing the metallic stub at $p_1 = 1$ mm, measured from the edge of the ground plane, provides the optimum configuration, enabling the antenna to resonate within the desired ISM band with excellent impedance matching. It can be observed that varying the stub position (p_1) significantly affects both the impedance matching and the isolation characteristics of the antenna. When the stub is positioned at $p_1 = 1$ mm, the antenna exhibits optimum resonance while maintaining the highest inter-element isolation. As the stub position is increased beyond this value, the resonant frequency shifts and both the impedance matching and isolation performance gradually deteriorate due to the weakened electromagnetic coupling between the parasitic stub and the radiating elements. Figure 10b presents the corresponding S_{12} characteristics, which further confirm that $p_1 = 1$ mm provides the best isolation performance. To further enhance inter-element isolation, a second parametric analysis was performed on the stub length (l_1), as illustrated in Figure. 11a for the S_{11} characteristics and Figure. 11b for the S_{12} characteristics. The length was varied from 17 mm to 20 mm, with an optimized value of $l_1 = 19$ mm, which not only ensured ISM band resonance but also improved the isolation. The stub length (l_1) directly determines the electrical length of the parasitic resonator and plays a significant role in the antenna performance. A shorter stub provides insufficient suppression of the coupling currents, whereas an excessively long stub shifts the resonant frequency and deteriorates the impedance matching characteristics. An optimized stub length of $l_1 = 19$ mm provides the best trade-off between impedance bandwidth and inter-element isolation by effectively suppressing the coupling currents while preserving the desired operating band. In addition, the effect of the stub width (w_1) was investigated, as illustrated in Figure 12. The stub width was varied from 0.4 mm to 1 mm to examine its influence on the impedance

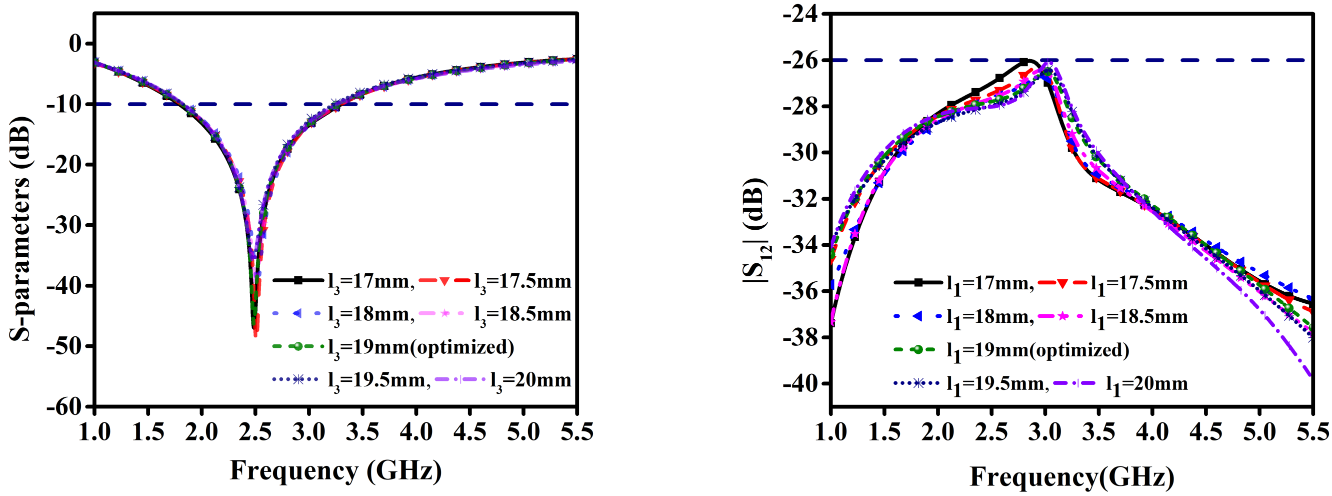

(a)

(b)

FIGURE 11: (a) S_{11} characteristics for the parametric analysis of stub length (l_1) from 17 mm to 20 mm. (b) Corresponding S_{12} characteristics showing isolation improvement.

matching, operating bandwidth, and inter-element isolation. It can be observed that the stub width significantly affects the electromagnetic coupling between the parasitic element and the radiating elements. Increasing the stub width alters the surface current distribution and the input impedance, resulting in changes to the resonant frequency and isolation performance. An optimized width of $w_1 = 0.5$ mm provides the best impedance matching within the ISM band while maintaining inter-element isolation below -27 dB. These results demonstrate that the stub width is a critical design parameter for achieving an optimal balance between impedance bandwidth and isolation performance.

The simulated S-parameters of the suggested MIMO antenna after the parametric analysis of l_1, w_1, and p_1 are presented in Figure. 13. The results reveal that incorporating the isolation element enables an operating bandwidth from 1.81 GHz to 3.27 GHz, with a resonance at 2.48 GHz achieving a return loss of 48 dB. The inter-element isolation is maintained below -26 dB across the entire operating band. For a quantitative comparison, the performance of the proposed four-port MIMO antenna before and after incorporating the metallic parasitic stub is summarized. Without the isolation structure, the antenna exhibits an impedance bandwidth of 1.76–3.49 GHz with a resonance at 2.48 GHz and an inter-element isolation of approximately -24 dB. After introducing the optimized metallic stub, the antenna maintains a comparable impedance bandwidth of 1.81–3.27 GHz while the return loss improves from approximately -29 dB to -48 dB. More importantly, the inter-element isolation is enhanced from approximately -24 dB to approximately -27 dB, corresponding to an improvement of about 3 dB. This quantitative comparison demonstrates that the proposed parasitic stub effectively suppresses mutual coupling between adjacent antenna elements without significantly affecting the impedance bandwidth, thereby improving the overall MIMO performance. As illustrated in Figure. 14, the simulated and practical S-parameters of the suggested four-port MIMO antenna correspond to Port 1 excitation. The minor discrepancies observed between the simulated and measured results can be attributed to fabrication tolerances and measurement uncertainties. Fabrication tolerances include slight variations in the PCB etching process, substrate dimensions, SMA connector soldering, and the dielectric properties of the FR4 substrate. In addition, measurement uncertainties associated with VNA calibration, connector alignment, and the anechoic chamber setup may also contribute to small deviations in the measured antenna characteristics. Nevertheless, the measured results exhibit good agreement with the simulated results, confirming the robustness and reliability of the proposed antenna under practical fabrication and measurement conditions. For brevity, the results for the remaining ports are not shown, as they exhibit similar characteristics. A strong agreement between the simulated and measured data confirms the validity of the proposed design.

Concerning MIMO diversity parameters The Envelope Correlation Coefficient (ECC) is a parameter used to evaluate the diversity performance of MIMO antennas.It measures how closely the signals received (or transmitted) at two different antenna ports are correlated in both phase and amplitude. Lower ECC values indicate higher independence between the radiation patterns, which leads to improved diversity gain and reduced signal fading. ECC can be obtained by integrating the normalized complex radiation fields over

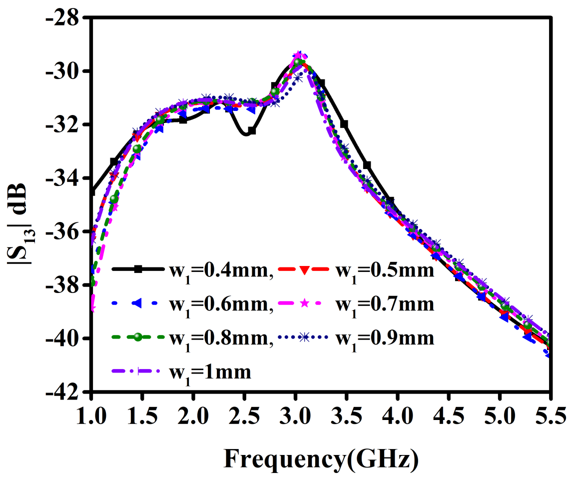

FIGURE 12: Parametric analysis of w_1 from 0.4 mm to 1 mm

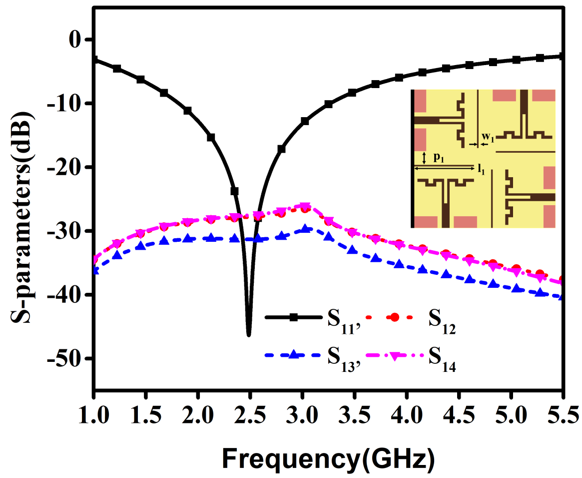

FIGURE 13: Simulated S-parameter results of the proposed Four-port MIMO antenna

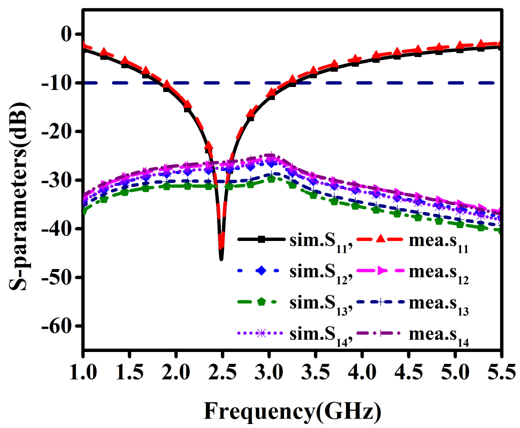

FIGURE 14: Simulated and experimental results of the suggested four-MIMO antenna

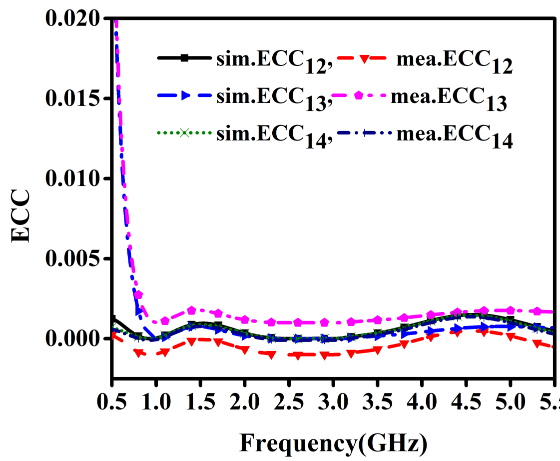

FIGURE 15: Simulated and practical Envelope Correlation Coefficient (ECC) of the suggested antenna.

the entire sphere, as expressed in eq (2):

$$\mathrm{ECC}_{ij} = \frac{\left| \int_0^{2\pi}\int_0^{\pi} \left[\vec{F}_i(\theta,\phi)\cdot\vec{F}_j^*(\theta,\phi)\right]\sin\theta\, d\theta\, d\phi \right|^2}{\left(\int_0^{2\pi}\int_0^{\pi} |\vec{F}_i(\theta,\phi)|^2 \sin\theta\, d\theta\, d\phi\right)} \times \frac{1}{\left(\int_0^{2\pi}\int_0^{\pi} |\vec{F}_j(\theta,\phi)|^2 \sin\theta\, d\theta\, d\phi\right)}. \quad (2)$$

Here, $\mathbf{F}_i(\theta,\phi)$ represents the complex vector far-field of the i-th antenna port, and $P(\theta,\phi)$ is the angular power distribution of the incoming signal, generally assumed to be isotropic ($P(\theta,\phi) = 1$) [28]. In the proposed design, both simulated and measured envelope correlation coefficient (ECC) values remain below 0.01 across the entire operating frequency range, as indicated in Figure. 15. This low ECC indicates excellent isolation between antenna elements and confirms the antenna's superior diversity performance. Diversity Gain (DG) quantifies the improvement in link reliability provided by the MIMO system under multipath conditions. It is directly related to ECC, with higher DG achieved when ECC is low. The relationship is expressed in as [29]:

$$\mathrm{DG} = 10\sqrt{1-\rho_e^2} \quad (\mathrm{dB}). \quad (3)$$

In the suggested antenna, the diversity gain (DG) values remain consistently close to 9.99 dB throughout the operating band, as illustrated in Figure. 16. This indicates robust diversity performance and effective signal reception in multipath environments. Mean Effective Gain (MEG) represents the average received power at a given antenna port, considering the incident signal environment [30]. It is defined as:

$$\mathrm{MEG}_i = \frac{1}{4\pi}\int_0^{2\pi}\int_0^{\pi} P(\theta,\phi)\, G_i(\theta,\phi)\, \sin\theta\, d\theta\, d\phi \quad (4)$$

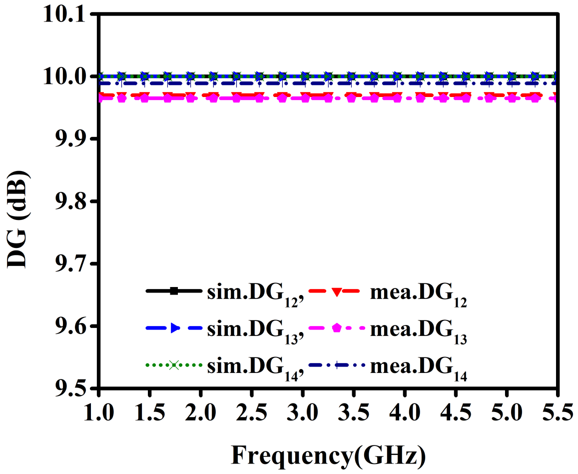

FIGURE 16: Simulated and practical Diversity Gain (DG) of the proposed antenna.

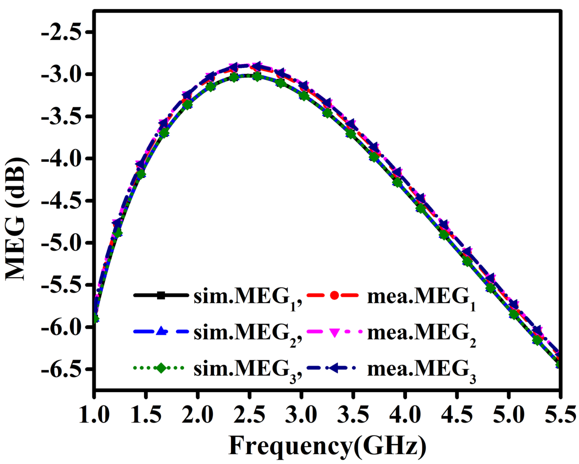

FIGURE 17: Simulated and practical Mean Effective Gain (MEG) of the suggested antenna.

where $G_i(\theta, \phi)$ is the gain pattern of the i-th port. For balanced MIMO operation, the mean effective gain (MEG) ought to be close to -3 dB, and the difference between MEG values of different ports should not exceed 3 dB. In our design, the MEG values remain below -3 dB across the operating band, as indicating in Figure. 17, indicating balanced power reception among all ports. Channel Capacity Loss (CCL) quantifies the reduction in the achievable MIMO channel capacity due to the correlation and mutual coupling between antenna ports [31]. It is calculated from the receive correlation matrix $\mathbf{\Psi}_R$ as

$$\text{CCL} = -\log_2 \left(\det \mathbf{\Psi}_R\right) \quad \text{(bits/s/Hz)}. \tag{5}$$

where $\mathbf{\Psi}_R$ is the receive correlation matrix obtained from the measured or simulated S-parameters of the MIMO antenna. For the proposed four-port MIMO antenna, the channel capacity loss was evaluated for different antenna-port combinations. In the corresponding figures, the indices i and

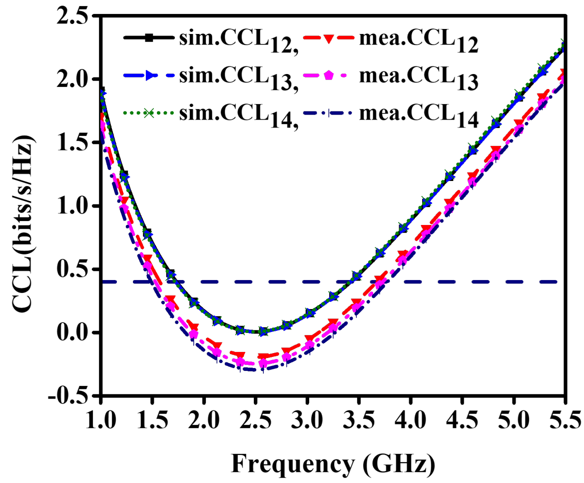

FIGURE 18: Simulated and practical Channel Capacity Loss (CCL) of the suggested antenna.

j denote the antenna port numbers $(i, j = 1, 2, 3, 4)$. For example, CCL_{12}, CCL_{13}, and CCL_{14} represent the channel capacity loss evaluated for the antenna-port pairs (1,2), (1,3), and (1,4), respectively. Acceptable CCL values are generally below 0.4 bits/s/Hz. As shown in Fig. 18, all evaluated CCL values remain below 0.36 bits/s/Hz across the operating band, indicating negligible channel capacity degradation and excellent MIMO performance. Fig. 19 illustrates TARC of the proposed MIMO antenna. TARC is an important performance metric that evaluates the overall reflection characteristics of a MIMO antenna under simultaneous multi-port excitation and is defined by Eq. (6)

$$\text{TARC} = \sqrt{\frac{\sum_{i=1}^{N} |b_i|^2}{\sum_{i=1}^{N} |a_i|^2}}, \tag{6}$$

where a_i and b_i denote the incident and reflected waves at the i^{th} port, respectively, and N is the total number of antenna ports. The TARC remains below -10 dB across the entire operating frequency band, indicating good active impedance matching, low reflected power, and efficient radiation performance under simultaneous excitation of all antenna ports. The simulated and measured radiation pattern characteristics of the proposed antenna at 1.94, 2.48, 2.89, and 3.20 GHz are presented in Fig. 20. These frequencies were selected as representative points across the operating band to experimentally validate the radiation performance of the antenna. The antenna exhibits stable E-plane and H-plane radiation patterns throughout the operating band, with good agreement between the simulated and measured results. The minor discrepancies observed are mainly attributed to fabrication tolerances, SMA connector soldering, and measurement uncertainties, thereby confirming the robustness and reliability of the proposed antenna.

The radiation characteristics of the suggested antenna are depicted in the polar plots shown in Figure. 21. The radiation

TABLE 1: Performance Comparison of Recent MIMO Antennas with Proposed Work

Reference (Year)	Size (mm^3)	Freq. (GHz)	S_{21} (dB)	ECC / DG	MEG (dB)	Eff. (%)
[32] (2025)	48×48×1.2	3.05–5.65	–25	0.012 / 9.89	–1.0	74–86
[31] (2025)	50×20×1.6	3.74–5.80	–45.5	0.004 / 9.99	—	75
[33] (2026)	100×100×1.6	2.4–3.5	-17	0.001/9.99	—3	95
[34] (2025)	70×70×1.4	5.4–20	-20	0.008/ -	-	80
[35] (2026)	62×62×0.25	3.84–4.32	–23	0.002 / 9.99	-	-
[36] (2024)	66×66×0.13	3.20–4.12	–20	0.005 / 9.95	–3	99
[37] (2026)	90×84×1.6	7.62–11.6	–20	0.004 / -	-	87
[38] (2025)	50×50×1.6	3.2–3.4	–23	0.0001 / 9.99	–3.0	94
Proposed work	45×45×1.6	1.8–3.87	–27	0.01/ 9.99	–3.0	96

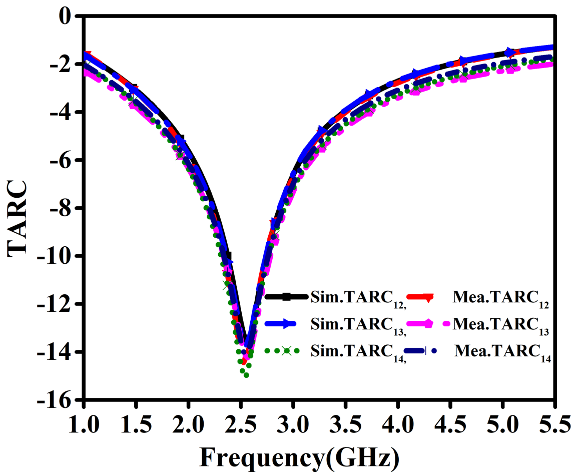

FIGURE 19: Simulated and practical TARC of the suggested antenna.

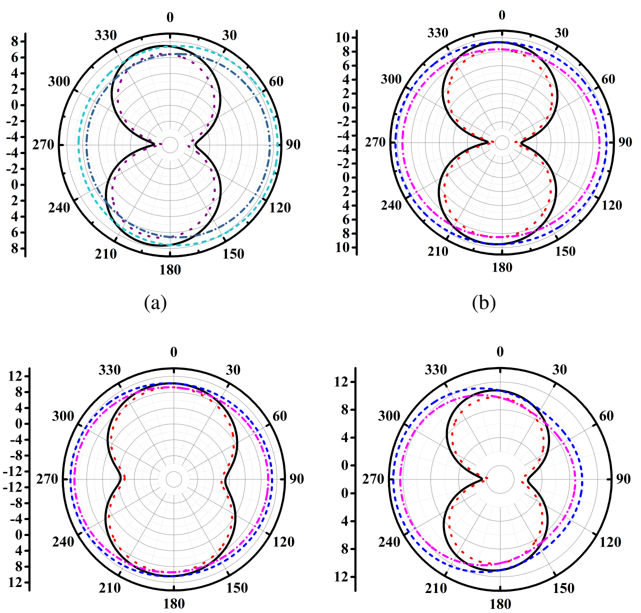

(a) (b) (c) (d)

FIGURE 20: Radiation patterns (simulated and practical) for different configurations: (a) 1.94 GHz (b) 2.48 GHz (c) 2.89 GHz (d) 3.20 GHz

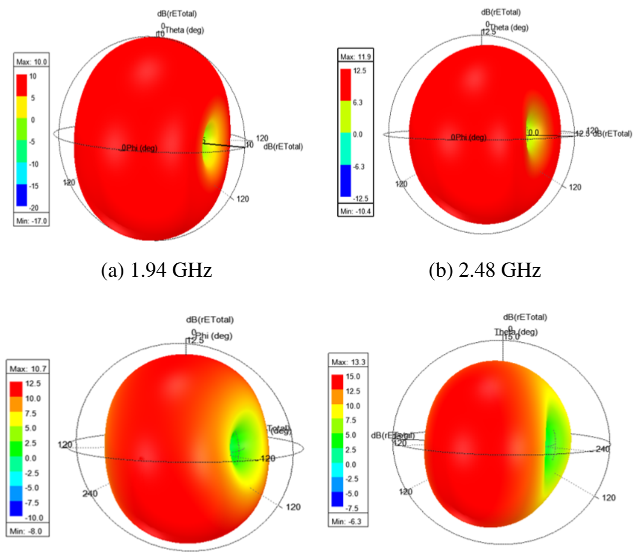

(a) 1.94 GHz (b) 2.48 GHz (c) 2.89 GHz (d) 3.20 GHz

FIGURE 21: Simulated and practical radiation patterns (polar plots) of the proposed antenna at (a) 1.94 GHz, (b) 2.48 GHz, (c) 2.89 GHz, and (d) 3.20 GHz.

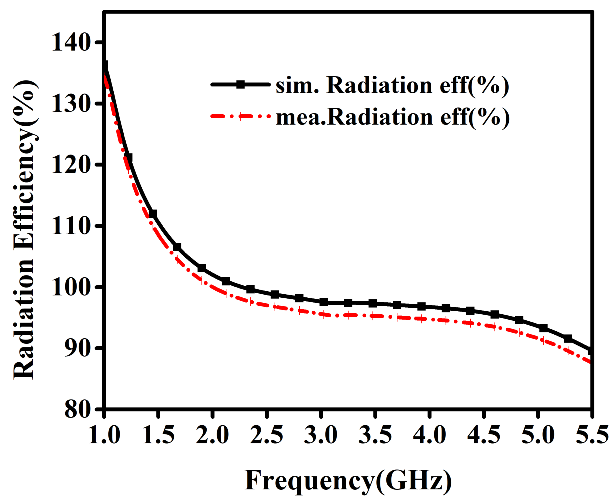

FIGURE 22: radiation efficiency of proposed Four-port MIMO antenna

efficiency of the suggested four-port MIMO antenna across the operating frequency range is illustrated in Figure 22 illustrates the simulated radiation efficiency of the proposed four-port MIMO antenna over the operating frequency range. A maximum simulated radiation efficiency of approximately 96% is achieved at the operating frequency. Although the radiation efficiency was not measured directly, the measured radiation patterns and gain show good agreement with the simulated results, thereby supporting the overall antenna performance. These results confirm that the proposed antenna provides adequate gain and high radiation efficiency for practical wireless communication applications.

Table 1 presents a detailed performance comparison between the proposed MIMO antenna and recently reported MIMO antennas operating in similar frequency bands and application scenarios. The comparison examines essential parameters such as physical size, operating frequency range, isolation level (S_{21}), envelope correlation coefficient (ECC), diversity gain (DG), mean effective gain (MEG), and peak gain/radiation efficiency.

Based on the comparison presented in Table 1, the proposed antenna offers several advantages over recently reported MIMO antennas. The proposed design achieves a compact size of $45 \times 45 \times 1.6$ mm^3, a wide impedance bandwidth (1.81–3.37 GHz), high inter-element isolation of up to -27 dB, low ECC (< 0.01), high radiation efficiency (96%), and excellent diversity performance using a simple metallic parasitic stub without requiring complex decoupling structures such as defected ground structures (DGS), electromagnetic bandgap (EBG) structures, or neutralization lines. This simple planar configuration facilitates low-cost fabrication and practical implementation. However, the proposed antenna also has certain limitations. The peak realized gain is relatively moderate (2.83 dBi) compared with some recently reported high-gain MIMO antennas. Furthermore, the design is optimized specifically for ISM-band applications, and its applicability to multiband or wideband wireless systems requires further investigation. These aspects will be considered in future work. Overall, the proposed antenna demonstrates competitive performance in terms of compactness, impedance bandwidth, isolation, radiation efficiency, and MIMO diversity characteristics, making it a suitable candidate for 2.4 GHz ISM-band wireless communication applications.

IV. CONCLUSION

This work has demonstrated the design and analysis of a compact four-port MIMO antenna optimized for the 2.4 GHz ISM band and compatible wireless communication systems. The antenna is implemented on an FR4 substrate using a coplanar waveguide feeding structure. To enhance isolation, a parasitic element is positioned between the radiating elements, resulting in a maximum isolation of -27 dB. The prototype achieves an impedance bandwidth spanning 1.81–3.37 GHz with superior impedance matching of -49 dB. It offers a measured peak gain of 2.83 dBi and a radiation efficiency of 96%. Evaluated MIMO diversity metrics, including an ECC below 0.01, a DG of 9.99 dB, a CCL of 0.36 bits/s/Hz, and an MEG below -3 dB, fall well within the accepted limits for high-performance MIMO systems. The strong correlation between simulated and measured results validates the effectiveness of the design, confirming its suitability for robust and efficient ISM band applications.

ACKNOWLEDGMENT

The management of VIT University and the School of Electronics Engineering (SENSE) department are acknowledged for their tremendous support and encouragement throughout this endeavor by the authors.

AUTHORSHIP CONTRIBUTION STATEMENT

Both authors have the same contributions

FUNDING

Not applicable.

Data Availability

No datasets were generated or analysed during the current study.

Competing Interests

The authors declare no competing interests.

REFERENCES

[1] A. E. Abdelsalam, O. M. Elghandour, E. S. Oda, and A. E. Magdy, "Analysis on different decoupling methods for mimo antenna in ultra-wide band applications: A review," Suez Canal Engineering, Energy and Environmental Science, vol. 3, no. 1, pp. 26–42, 2025.

[2] N. V. Deshpande, M. R. Castellanos, S. R. Khosravirad, J. Du, H. Viswanathan, and R. W. Heath Jr, "Beamforming with hybrid reconfigurable parasitic antenna arrays," arXiv preprint arXiv:2502.17864, 2025.

[3] I. Gnanaharan and R. Anbazhagan, "Review on the design of the isolation techniques for uwb-mimo antennas," Advanced Electromagnetics, vol. 7, no. 4, p. 46–70, 2018.

[4] M. Salehi and H. Oraizi, "Wideband high gain metasurface-based 4t4r mimo antenna with highly isolated ports for sub-6 ghz 5g applications," scientific reports, vol. 14, no. 1, p. 14448, 2024.

[5] M. R. K. M. Samy and A. Gudipalli, "Design circular polarized antenna at ism band for wban using parasitic elements," Heliyon, vol. 10, no. 6, 2024.

[6] M. A. Sufian, N. Hussain, A. Abbas, J. Lee, S. G. Park, and N. Kim, "Mutual coupling reduction of a circularly polarized mimo antenna using parasitic elements and dgs for v2x communications," IEEE Access, vol. 10, pp. 56388–56400, 2022.

[7] K. D. Ayinala and P. K. Sahu, "Isolation enhanced compact dual-mode 4-port mimo design using slot-based switchable dgs decoupling filters," Wireless Personal Communications, vol. 135, no. 2, pp. 805–833, 2024.

[8] T. Vijetha, D. Ramakrishna, and K. Bharath, "Dual polarized reconfigurable mimo antenna for multi-band functioning," Advanced Electromagnetics, vol. 13, no. 2, pp. 1–15, 2024.

[9] P. Tiwari, V. Gahlaut, M. Kaushik, A. Shastri, V. Arya, I. Elfergani, C. Zebiri, and J. Rodriguez, "Enhancing performance of millimeter wave mimo antenna with a decoupling and common defected ground approach," Technologies, vol. 11, no. 5, p. 142, 2023.

[10] P. Kumar, R. Sinha, A. Choubey, and S. K. Mahto, "Dgs based miniaturized wideband mimo antenna with efficient isolation for c band applications," Frequenz, vol. 77, no. 3-4, pp. 163–172, 2023.

[11] A. M. Saleh, T. A. Nagim, R. A. Abd-Alhameed, J. M. Noras, and C. H. See, "Mutual coupling reduction of dual-band uni-planar mimo system using neutralization line technique," Applied Computational Electromagnetics Society Journal (ACES), pp. 176–186, 2020.

[12] T. Wu and J.-W. Wang, "Neutralization-line-based decoupling for miniaturized mimo antenna array," Microwave and Optical Technology Letters, vol. 65, no. 2, pp. 685–689, 2023.
[13] K. S. Muttair, A. Z. G. Zahid, O. A. Shareef, A. M. Q. Kamil, and M. F. Mosleh, "A novel design of wide and multi-bands 2× 2 multiple-input multiple-output antenna for 5g mm-wave applications," International Journal of Electrical and Computer Engineering, vol. 12, no. 4, pp. 3882–3890, 2022.
[14] K. S. Muttair, K. K. Aljawaheri, M. Z. Ali, O. A. Shareef, and M. F. Mosleh, "New ultra-small design and high performance of an 8× 8 massive mimo antenna for future 6g wireless devices," Indonesian Journal of Electrical Engineering and Computer Science, vol. 28, no. 1, pp. 587–599, 2022.
[15] K. S. S. Muttair, "Novel fractal geometry of 4× 4 multi-input and multi-output array antenna for 6g wireless systems," 2023.
[16] K. S. Muttair, O. A. Shareef, H. B. Taher, and F. Arith, "A new geometry of multi-band mimo antenna for 5g and 6g systems," Journal of Techniques, vol. 6, no. 4, pp. 48–56, 2024.
[17] K. S. Muttair, A. Z. G. Zahid, O. A. Shareef, R. H. C. Alfilh, A. M. Q. Kamil, and M. F. Mosleh, "Design and analysis of wide and multi-bands multi-input multi-output antenna for 5g communications," Indonesian Journal of Electrical Engineering and Computer Sciences, vol. 26, no. 2, pp. 903–914, 2022.
[18] A. Omrani, "An ultra-wideband microstrip mimo antenna with ebg loading for wlan and sub-6g applications," arXiv preprint arXiv:2303.00530, 2023.
[19] S. Dey, S. Dey, and S. K. Koul, "Isolation improvement of mimo antenna using novel ebg and hair-pin shaped dgs at 5g millimeter wave band," IEEE Access, vol. 9, pp. 162820–162834, 2021.
[20] T. Upadhyaya, V. Sorathiya, S. Al-Shathri, W. El-Shafai, U. Patel, K. V. Pandya, and A. Armghan, "Quad-port mimo antenna with high isolation characteristics for sub 6-ghz 5g nr communication," Scientific Reports, vol. 13, no. 1, p. 19088, 2023.
[21] A. Bhowal and S. Aïssa, "Mimo device-to-device communications via cooperative dual-polarized intelligent surfaces," IEEE Wireless Communications Letters, vol. 12, no. 2, pp. 202–206, 2022.
[22] M. Hussain, W. Awan, E. Ali, M. Alzaidi, M. Alsharef, D. Elkamchouchi, A. Alzahrani, and M. F. A. Sree, "Isolation improvement of parasitic element-loaded dual-band mimo antenna for mm-wave applications. micromachines 2022; 13: 1918," IJACSA) International Journal of Advanced Computer Science and Applications, 2022.
[23] J. Sui, C. Huang, J. Li, X. Zhu, and D. Li, "Wideband aperture-overlapped mimo antennas naturally integrating mode orthogonal and parasitic decoupling schemes," IEEE Antennas and Wireless Propagation Letters, vol. 23, no. 8, pp. 2441–2445, 2024.
[24] T. Addepalli and V. Anitha, "Parametric analysis of compact uwb-mimo antenna with improved isolation using parasitic reflectors and protruded ground strips," Wireless Personal Communications, vol. 123, no. 3, pp. 2209–2225, 2022.
[25] K. Zhang, Y. Li, Q. Yuan, G. Sun, and Y. Wang, "W-band wideband high-gain circularly polarized π-shaped antenna array with stacked parasitic patches," Microelectronics Journal, p. 106729, 2025.
[26] M. Li and S. Cheung, "A novel calculation-based parasitic decoupling technique for increasing isolation in multiple-element mimo antenna arrays," IEEE Transactions on Vehicular Technology, vol. 70, no. 1, pp. 446–458, 2020.
[27] Y. Chung, S.-S. Jeon, D. Ahn, J.-I. Choi, and T. Itoh, "High isolation dual-polarized patch antenna using integrated defected ground structure," IEEE Microwave and Wireless Components Letters, vol. 14, no. 1, pp. 4–6, 2004.
[28] M. A. Jensen and J. W. Wallace, "A review of antennas and propagation for mimo wireless communications," IEEE Transactions on Antennas and propagation, vol. 52, no. 11, pp. 2810–2824, 2004.
[29] H. Tran-Huy, H. N. Tuan, N. Q. Dinh, D.-N. Tran-Viet, and H.-C. Park, "Multi-element self-decoupled mimo patch antenna with flexible characteristics," IEEE Access, vol. 12, pp. 21569–21575, 2024.
[30] T. Taga, "Analysis for mean effective gain of mobile antennas in land mobile radio environments," IEEE Transactions on Vehicular Technology, vol. 39, no. 2, pp. 117–131, 2002.
[31] M. Himaja, S. Yuvaraj, and P. Kishore Kumar, "An integrable high isolation mimo antenna for wireless and ism band applications: design and evaluation," Wireless Networks, vol. 31, no. 6, pp. 4363–4376, 2025.
[32] A. Kumar Saurabh, P. Singh Rathore, and M. Kumar Meshram, "Compact wideband four-element mimo antenna with high isolation," Electronics Letters, vol. 56, no. 3, pp. 117–119, 2020.
[33] P. Thanki, T. Upadhyaya, U. Patel, K. Aliqab, M. Alsharari, A. A. Althuwayb, A. Armghan, and V. Sorathiya, "Dual band four port mimo antenna with dual circular polarization for wi-fi/wimax applications," Alexandria Engineering Journal, vol. 112, pp. 1–16, 2025.
[34] Q. Zhou, Z. Wang, W. Nie, C. Li, Y. Tao, and W. Ren, "High-isolation ultra-wideband mimo antenna based on sunflower-shaped radiating patch and defected ground structure," Prog. Electromagn. Res. M, vol. 157, pp. 129–138, 2025.
[35] F. Younis, A. H. Jabire, J. Ahmad, A. El Ansari, H. Luo, and S. Wang, "Compact quad-port mimo antenna with intrinsic self-decoupling and high isolation for ism/wlan at 2.45 ghz: F. younis et al.," Journal of Electronic Materials, vol. 55, no. 2, pp. 2419–2433, 2026.
[36] R. N. Tiwari, P. Singh, B. K. Kanaujia, and K. Srivastava, "Neutralization technique based two and four port high isolation mimo antennas for uwb communication," AEU-International Journal of Electronics and Communications, vol. 110, p. 152828, 2019.
[37] F. Younis, A. H. Jabire, J. Ahmad, O. Khan, M. J. Qasim, S. Mustafa, H. Luo, and S. Wang, "Hybrid electromagnetic decoupling-based isolation enhanced compact mimo antenna for ism-band wireless systems," Wireless Personal Communications, pp. 1–26, 2026.
[38] M. Bose and V. Karuppiah, "Metamaterial inspired superstrate loaded miniaturized quad port mimo antenna for 5g c-band applications," Optics Communications, vol. 574, p. 131123, 2025.